RESEARCH ARTICLE | JULY 21 2025

Multimodal azimuthal oscillations in electron beam generated $\boldsymbol{E}\times\boldsymbol{B}$ plasma



Phys. Plasmas 32, 073511 (2025) https://doi.org/10.1063/5.0273397





Articles You May Be Interested In

Anticathode effect on multimodal azimuthal oscillations in electron beam generated E × B plasma

Appl. Phys. Lett. (February 2025)

Excitation of the modified Simon-Hoh instability in an electron beam produced plasma

Phys. Fluids B (June 1993)

Growth and nonlinear evolution of the modified Simon-Hoh instability in an electron beam-produced plasma

Phys. Plasmas (May 2000)



Published Online: 21 July 2025

Multimodal azimuthal oscillations in electron beam generated E×B plasma

Cite as: Phys. Plasmas **32**, 073511 (2025); doi: 10.1063/5.0273397 Submitted: 30 March 2025 · Accepted: 26 June 2025 ·







Nirbhav Singh Chopra,^{1,2,a)} (b) Mina Papahn Zadeh,³ (b) Mikhail Tyushev,³ (b) Andrei Smolyakov,³ (b) Alexandre Likhanskii,⁴ (b) and Yevgeny Raitses¹ (b)

AFFILIATIONS

- ¹Princeton Plasma Physics Laboratory, Princeton University, Princeton, New Jersey 08543, USA
- ²Department of Astrophysical Sciences, Princeton University, Princeton, New Jersey 08544, USA
- ³Department of Physics and Engineering Physics, University of Saskatchewan, Saskatoon Saskatchewan S7N 5E2, Canada
- ⁴Applied Materials Inc, 35 Dory Rd., Gloucester, Massachusetts 01930, USA

ABSTRACT

Electron beam (e-beam) generated plasmas with applied crossed electric and magnetic ($E \times B$) fields are promising for low-damage material processing. However, these plasmas can be subject to the formation of azimuthally propagating structures that enhance the radial transport of energetic charged species, which can harm the gentle processing capability of the plasma. In this work, we investigate the azimuthal structure formation in an e-beam generated $E \times B$ plasma using experimental diagnostics and 2D3V particle-in-cell simulations. Our findings demonstrate the formation of multiple simultaneously occurring azimuthally propagating modes that exhibit nontrivial radial dependence. It is suggested that the multimodal azimuthal spectrum is caused in part by the radial outflow of ions in the plasma.

© 2025 Author(s). All article content, except where otherwise noted, is licensed under a Creative Commons Attribution (CC BY) license (https://creativecommons.org/licenses/by/4.0/). https://doi.org/10.1063/5.0273397

I. INTRODUCTION

Electron beam (e-beam) generated plasmas with applied electric and magnetic (E \times B) fields are promising for applications requiring efficient generation of ions and radicals in low pressure environments. ^{1–7} A key capability of magnetically confined e-beam plasma sources is that they can generate reactive species while maintaining low energetic particle flux to substrates placed in the periphery of the plasma region. ^{8–11}

In many axisymmetric $E \times B$ plasma systems, such as Penning discharges, Hall discharges, sputtering magnetrons, and Bernas sources, electrons are magnetized (electron Hall parameter $\Omega_e = \omega_{ce}/\nu_e \gg 1$, where ω_{ce} and ν_e are the electron cyclotron and electron collision frequencies), while ions are usually non-magnetized (ion Hall parameter $\Omega_i = \omega_{ci}/\nu_i \ll 1$, where ω_{ci} and ν_i ion cyclotron and ion collision frequencies) or very weakly magnetized $(\Omega_i \lesssim 1)^{12-16}$ Therefore, ion transport is dominated by an ambipolar electric field and collisions with neutrals. Previous work on e-beam generated $E \times B$ Penning plasma has demonstrated the formation of an ion-confining radial electric potential well. This potential can be leveraged for low-damage threshold material processing applications by limiting

energetic ion flux, thereby preventing energetic ions from damaging material surfaces.

However, several operating regimes of axisymmetric $E\times B$ plasma devices are accompanied by large-scale azimuthally propagating fluctuations in plasma density and potential "spokes" induced by a modified Simon–Hoh instability (MSHI). $^{12,13,16-22}$ The spoke has been shown to energize ions in the radial direction, thereby reintroducing energetic ions to the peripheral substrate processing region. 23 Therefore, mitigating the formation of the spoke may enable a wider operating regime of gentle processing capability of the e-beam generated $E\times B$ plasma.

In this work, we experimentally and computationally investigate the structure and formation of azimuthally propagating plasma structures in an e-beam generated $E\times B$ plasma. Our experimental findings indicate the existence of two regions with distinct azimuthal mode formation. We also performed 2D3V particle-in-cell (PIC) simulations in the plane perpendicular to the applied magnetic field to independently determine the radial macroscopic profiles and azimuthal mode spectrum. Good agreement is shown between experimental findings and the simulation.

The paper is organized as follows: Sec. II discusses the experimental setup of the e-beam generated $E \times B$ plasma. Section III discussed

a) Author to whom correspondence should be addressed: nschopra@princeton.edu

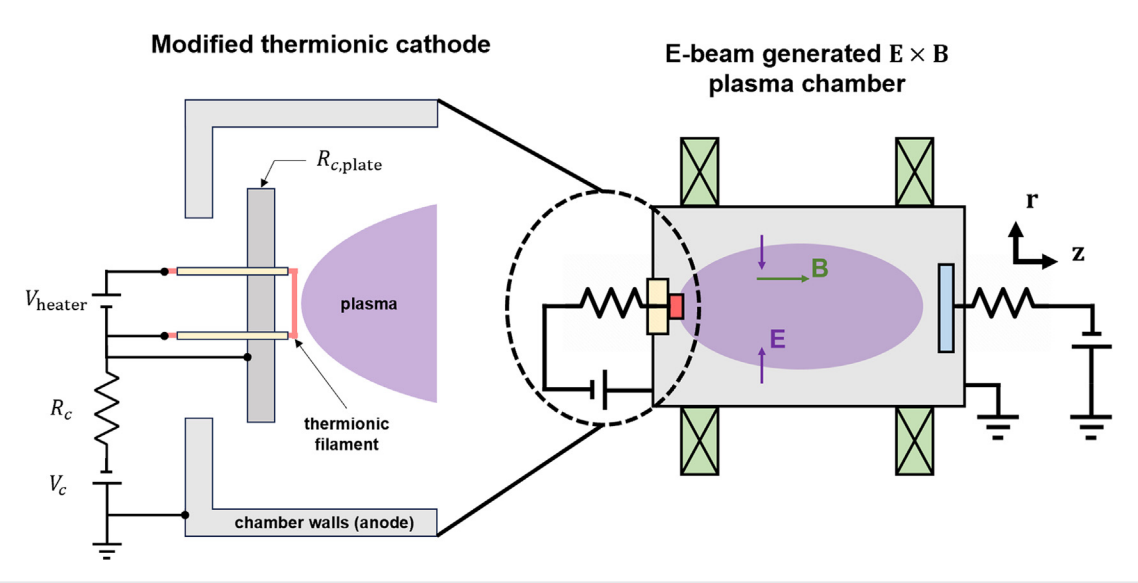


FIG. 1. Schematic of modified thermionic cathode installed on e-beam generated $\mathsf{E} \times \mathsf{B}$ chamber.

the plasma diagnostics and measurement procedures used, as well as the PIC simulation setup. Section IV details the results of the probe measurements and their analysis, as well as the experimental validation of the PIC simulations. Analytical models of the radial electron and ion transport and azimuthal instability onset are proposed and compared to the experimental measurements in Sec. V. Conclusions are summarized in Sec. VI.

II. EXPERIMENTAL SETUP

The experimental setup consisted of an e-beam generated $E \times B$ plasma chamber with a conducting anticathode installed on the axially

opposite side of the chamber from the cathode. The setup used in this work is nearly identical to the setup described in Ref. 24 and is briefly described here. The e-beam chamber is a cylindrical vacuum vessel that is pumped by a turbomolecular pump backed by a rough pump to a base pressure of $\sim\!\!1\,\mu{\rm Torr}.$ The chamber is filled with Ar gas to a pressure of 0.1 mTorr. An axial magnetic field of 75–125 G is generated by electromagnets arranged in a Helmholtz-like configuration along the chamber. The anticathode has a radius of 4.5 cm.

However, in the present setup, the thermionic cathode was significantly modified, which is depicted in Fig. 1. The filament is made from a 0.4 mm diameter tungsten wire, which is ohmically heated

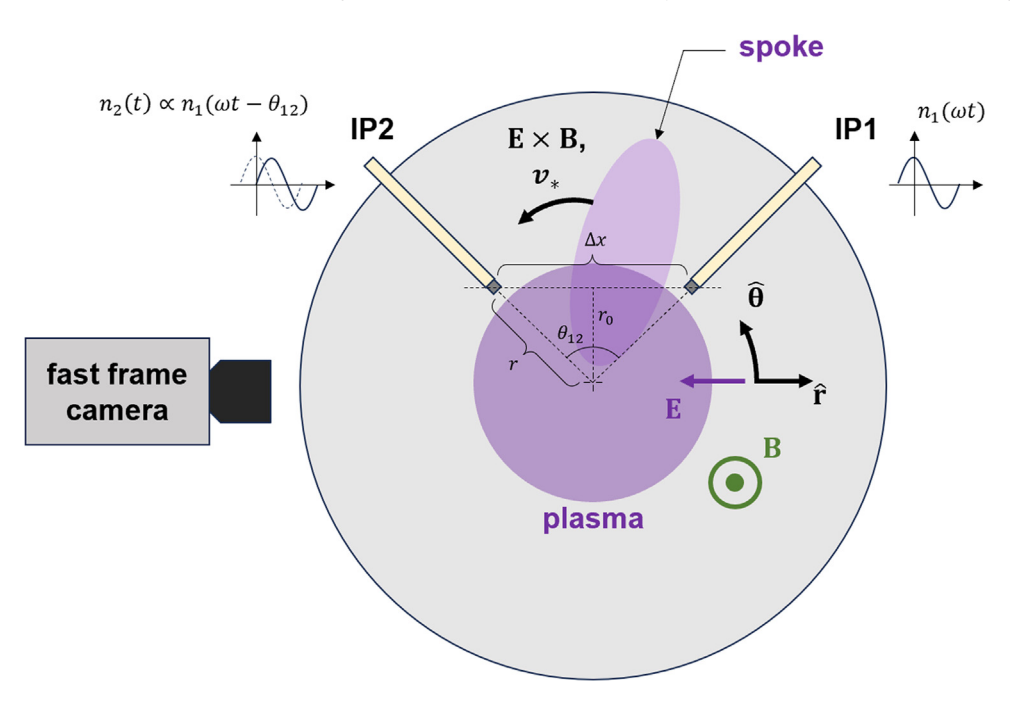


FIG. 2. Schematic of diagnostic setup for azimuthal oscillation characterization. The ebeam is injected in the $+\hat{z}$ direction. Also shown is the direction of E \times B and electron diamagnetic drift velocity v_* .

TABLE I. Geometric properties of the probe array.

r ₀ (cm)	r (cm)	θ ₁₂ (rad) (°)
1.0	1.5	1.6 (93°)
2.0	2.3	1.0 (55°)
3.0	3.2	0.7 (39°)

using a heater power supply with bias voltage $V_{\rm heater}$. The filament length is 10 mm. The filament assembly is inserted through a stainless-steel cathode plate with radius $R_{c,\rm plate}=4.5$ cm and is electrically isolated from the cathode plate with ceramic tubes so that heater current does not pass directly through the cathode plate body. Both the thermionic filament and the cathode plate are biased to the applied cathode bias voltage $V_c=-55$ V. The discharge current is measured using a current shunt on the cathode and is $I_d=100$ mA. The modified cathode increases the region of axial electron confinement to the radial extent of the cathode plate $R_{c,\rm plate}$.

In this work, the anticathode is biased to the cathode potential so that it is electron repelling, i.e., operated in "repeller mode" with anticathode bias potential $V_{atc} = V_c$. This is in contrast to "collector mode," whereby the anticathode is biased to the anode potential $V_{atc} = 0 \, \text{V}$ and therefore collects nearly all incident electrons. The effect of the anticathode operating in collector mode is not considered in the present work.

III. METHODS

A. Diagnostics and measurement procedure

A Langmuir probe (LP) and emissive probe (EP) diagnostic were mounted at the axial midplane of the chamber and were used to determine the electron energy distribution function (EEDF), electron density, electron temperature, and plasma potential at different radii. These diagnostics are described in further detail in Ref. 24.

The coherent azimuthal plasma density oscillations were determined by an azimuthally oriented ion probe array that was mounted

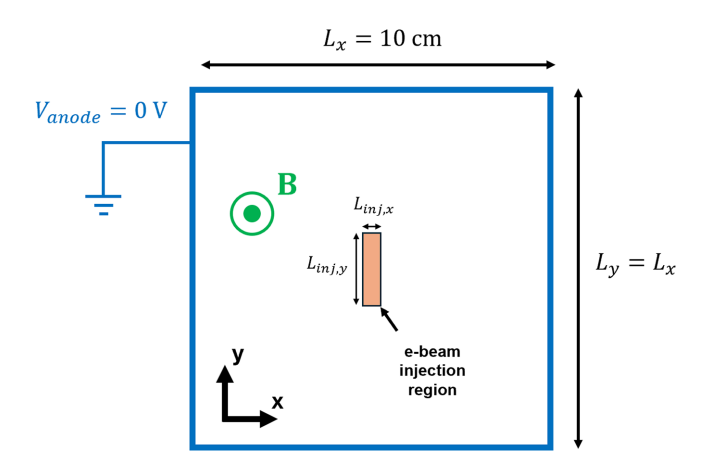
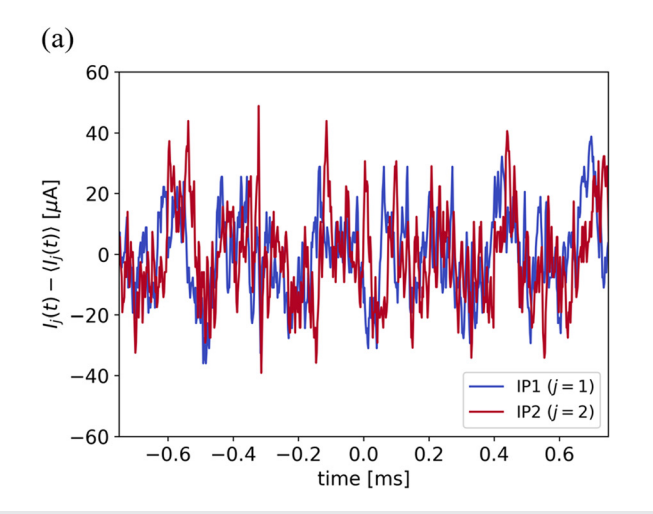


FIG. 4. Diagram of simulation domain.

at the axial midplane of the chamber (Fig. 2). The ion probe array consists of two negatively biased tungsten wires with identical exposed collecting areas, each with diameter 1.1 mm and exposed wire length of 1.7 mm. Each tungsten wire is inserted into a ceramic tube of outer diameter 2.1 mm. The probe tips are separated by a distance $\Delta x = 2.1$ cm such that the azimuthal angle subtended by the probe array is given by $\theta_{12} = 2 \arctan(\Delta x/2r_0)$, where r_0 is the probe array retraction depth. As a result, the radial distance of the probe tips to the geometric center of the plasma is given by $r = \sqrt{(\Delta x)^2 + r^2}$. The geometric

center of the plasma is given by $r = \sqrt{\left(\frac{\Delta x}{2}\right)^2 + r_0^2}$. The geometric properties of the probe array are shown in Table I.

The tungsten wire is individually biased to a potential of $V_b = -100\,\mathrm{V}$ relative to the grounded chamber walls, such that the probe ion collection is in an orbital motion limited (OML) regime. Under such conditions, the ion current I_j collected by the j th ion probe $[j=1\ \text{or}\ 2\ \text{corresponding}\ \text{to}\ \text{ion}\ \text{probe}\ 1\ \text{(IP1)}$, and ion probe 2 (IP2)] is independent of the electron temperature and is proportional to the local plasma density, $^{2.5,26}$



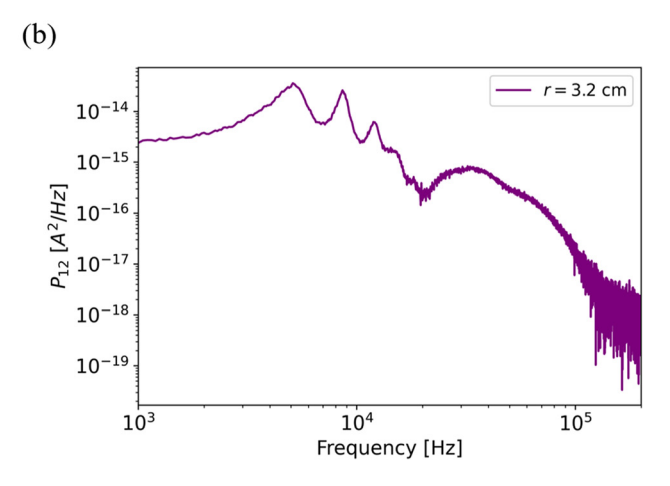


FIG. 3. (a) Ion current temporal signal $I_j(t)$ determined by IP1 (j=1) and IP2 (j=2) for B=100 G, $V_c=-55$ V, p=0.1 mTorr, with mean signal subtracted. (b) Cross spectral density P_{12} of I_1 and I_2 .

TABLE II. Parameters of the PIC simulations used in this work. Symbols used in this table: λ_{De} is the minimum electron Debye length; C is the maximum Courant number; $N_{\text{macro.}}$ is the number of physical particles per macroparticle; $L_{inj,x,y}$ is the side length of rectangular electron beam injection region in x, y direction; I_{inj} is the injected electron beam current; and ε_b is the injected electron beam energy.

Parameter	Value	
Δx	0.130 mm	
Δt	$1.7 \times 10^{-11} \mathrm{s}$	
λ_{De}	0.150 mm	
C	0.26	
$N_{ m macro.}$	1.0625×10^{7}	
$L_x = L_y$	10 cm	
$L_{inj,x}$	0.4 mm	
$L_{inj,x} \ L_{inj,y}$	10 mm	
I_{inj}	100 mA	
P	0.1 mTorr (Argon)	
B	100 G	
$arepsilon_b$	55 eV	

$$I_{j}(t) = \frac{2}{\sqrt{\pi}} e n_{j}(t) A_{pr} \sqrt{-\frac{e(V_{b} - V_{pl})}{2\pi m_{i}}},$$
 (1)

where $n_j(t)$ is the temporally fluctuating plasma density at the j th probe, A_{pr} is the probe collection area, V_{pl} is the plasma potential, and m_i is the Argon ion mass. Here, the plasma is assumed to be quasineutral, $n_j \approx n_i \approx n_e$ where n_i and n_e are the ion and electron densities, respectively.

A two point-correlation technique is used to determine the azimuthally coherent portion of the fluctuating signal collected by each ion probe. The cross power spectral density (CSD) is used to quantitatively determine the coherence and relative phase of $n_1(t)$ and $n_2(t)$. Representative ion current signals collected by IP1 and IP2 and their cross spectral density P_{12} are shown in Fig. 3. The CSD is defined as the Fourier transform of the cross correlation of the two signals, 28

$$P_{12}(f) \equiv \int_{-\infty}^{\infty} \left[\int_{-\infty}^{\infty} n_1(t) n_2(t+\tau) dt \right] e^{-i2\pi f \tau} d\tau$$

$$\equiv F \left(\int_{-\infty}^{\infty} n_1(t) n_2(t+\tau) dt \right), \tag{2}$$

where f is the frequency. The cross-coherence is defined as²⁸

$$C_{12}(f) \equiv \frac{|P_{12}|^2}{|P_{11}||P_{22}|},\tag{3}$$

which quantifies the fraction of spectral power transferred from n_1 to n_2 , for each spectral component f. Moreover, the argument of the CSD, $\operatorname{Arg}(P_{12})$, quantifies the relative phase between n_1 and n_2 for each spectral component f. Here, the argument function is taken to have the convention that for a complex valued function g, $\pi < \operatorname{Arg}(g) \le \pi$.

Azimuthal oscillations were also independently determined by a fast frame camera. A Phantom v7.3 high speed camera operating at 95 kfps imaged the optical emission of the plasma in the r-z plane (Fig. 2). The fast frame images were then averaged along the axial (z)

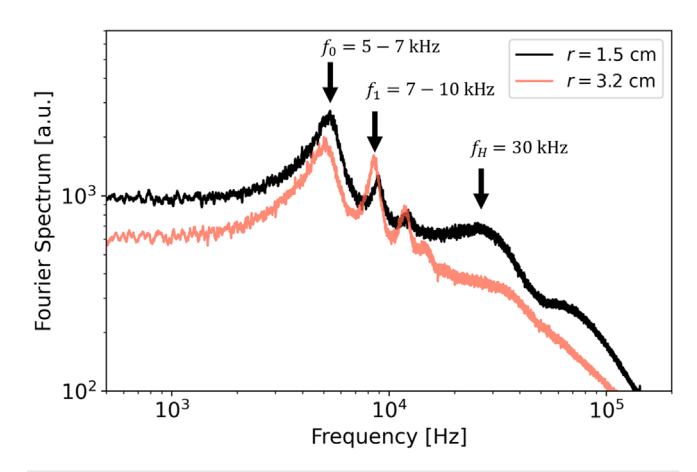


FIG. 5. FFT of ion density temporal trace determined by IP1, measured at r=1.5 and r=3.2 cm. Parameters are B=100 G, $V_c=-55$ V, p=0.1 mTorr.

direction and Fourier transformed in time to determine the radial dependence of the plasma emission oscillations.

B. Particle in-cell method

A 2D3V particle-in-cell method (PIC) was developed using the WarpX code²⁹ to simulate the electron beam generated $E \times B$ plasma in the plane perpendicular to the applied magnetic field and are similar to the simulations described in Ref. 30. The code is run on the Digital Research Alliance of Canada Mist server with one NVIDIA V100-SMX2-32GB GPU per simulation. The simulation domain is indicated in Fig. 4, and relevant simulation parameters are shown in Table II. Simulations were performed to most closely emulate the conditions of the experimental setup. One step electron-Argon impact ionization $(Ar + e \rightarrow Ar + e + e, Ref. 31)$, electron–Argon excitation $(Ar + e \rightarrow Ar^* + e, Ref. 32)$, and electron-Argon elastic (Ref. 33) scattering reactions were included. The simulation is initialized with an electron beam population that is injected into a background of neutral Argon. After an initial transient period, a self-consistent quasi steady-state discharge is sustained through the above-mentioned electron collisional processes and electron and ion losses to the absorbing boundary of the domain.

The major difference between the PIC setup and the experimental setup is the geometry of the anode in the computational domain, which is a square with side lengths $L_x = L_y = 10$ cm. This is compared to the experimental chamber, which is a cylindrical vacuum vessel with a diameter of $D_{\rm expt.} = 20$ cm. Azimuthal oscillations and time averaged radial profiles of electron density, temperature, and plasma potential are determined from the PIC simulations and are compared to the experimental measurements. The temporal spectra of the azimuthal oscillations occurring in the PIC simulations were determined by the multiple signal classification (MUSIC) super-resolution signal processing method. 23,34

IV. RESULTS

A. Experimental measurements

The Fourier spectra of the plasma density fluctuation $F(n_1(t))$ at r = 1.5 and 3.2 cm are shown in Fig. 5, for operating conditions

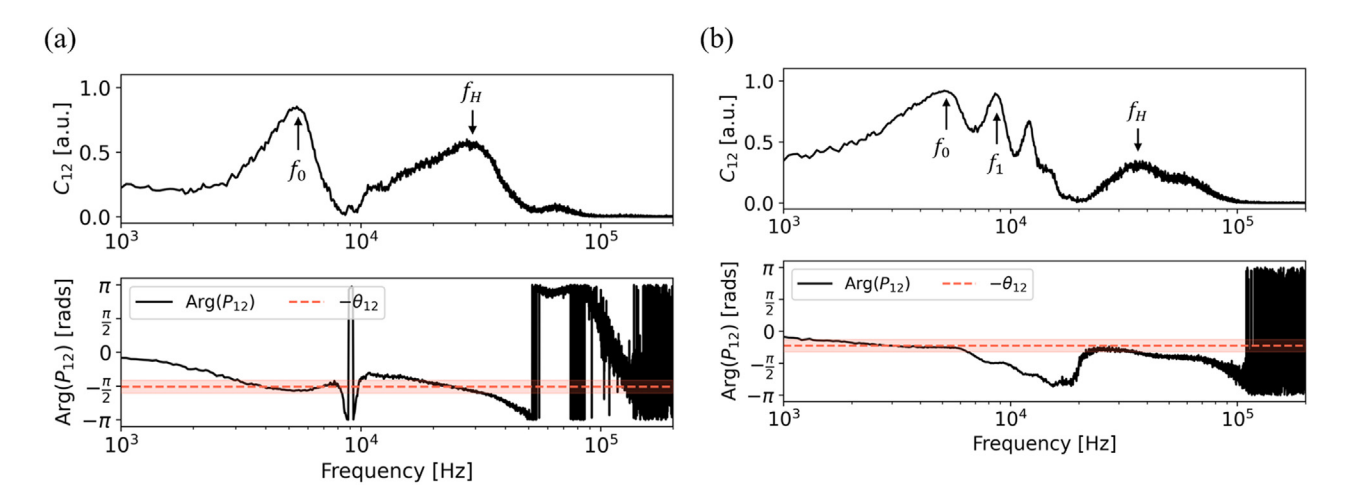


FIG. 6. Cross coherence and argument of cross spectral density of ion density temporal traces, measured at (a) r = 1.5 and (b) r = 3.2 cm. Parameters B = 100 G, p = 0.1 mTorr, $V_c = -55$ V. The modes f_0 , f_1 , and f_H are also labeled.

 $V_c=-55~{
m V},~B=100~{
m G},~p=0.1~{
m mTorr}.$ Both $r=1.5~{
m and}~r=3.2~{
m cm}$ measurements show prominent low frequency modes occurring at $f_0=5$ –7 kHz and the double frequency harmonic $f_1\approx 2f_0$, with f_1 increasing in amplitude at $r=3.2~{
m cm}$. There is also a higher frequency mode $f_H=30~{
m kHz}$ that is more prominent at $r=1.5~{
m cm}$.

The cross coherence of $n_1(t)$ and $n_2(t)$, $C_{12}(f)$ is shown in Fig. 6, for the same experimental parameters. Figures 6(a) and 6(b) indicate that at r=1.5 cm both low and high frequency modes at f_0 and f_H have a high coherence with $C_{12} > 0.5$. Moreover, both modes obey $Arg(P_{12}(f_0)) \approx Arg(P_{12}(f_H)) \approx -\theta_{12}$, indicating both f_0 and f_H are single-lobed (m=1) modes that are azimuthally propagating in the $+E \times B$ direction. At r=3.2 cm, the coherence of the low frequency mode remains high $C_{12}(f_0) > 0.8$, while the high frequency mode coherence reduces $C_{12}(f_H) < 0.5$. The

azimuthally propagating modes occurring at f_0 and f_H are also corroborated by the fast frame imaging diagnostic (Subsection 1 of the Appendix).

The cross-coherence dependence on the applied magnetic field is shown for r=1.5 and r=3.2 cm in Fig. 7. A trend of enhancement in the coherence of f_0 and f_1 and suppression of f_H can be observed for increasing magnetic field. This trend is also confirmed by the fast frame image analysis (Subsection 1 of the Appendix).

B. Experimental validation of 2D PIC model

A snapshot of the ion density computed by the PIC simulation after reaching quasi-steady state is shown in Fig. 8. Also shown are the azimuthal and radial components of the wavevector associated with the observed density wave, $\mathbf{k} = k_r \hat{\mathbf{r}} + k_\theta \hat{\theta}$. Indeed an azimuthally

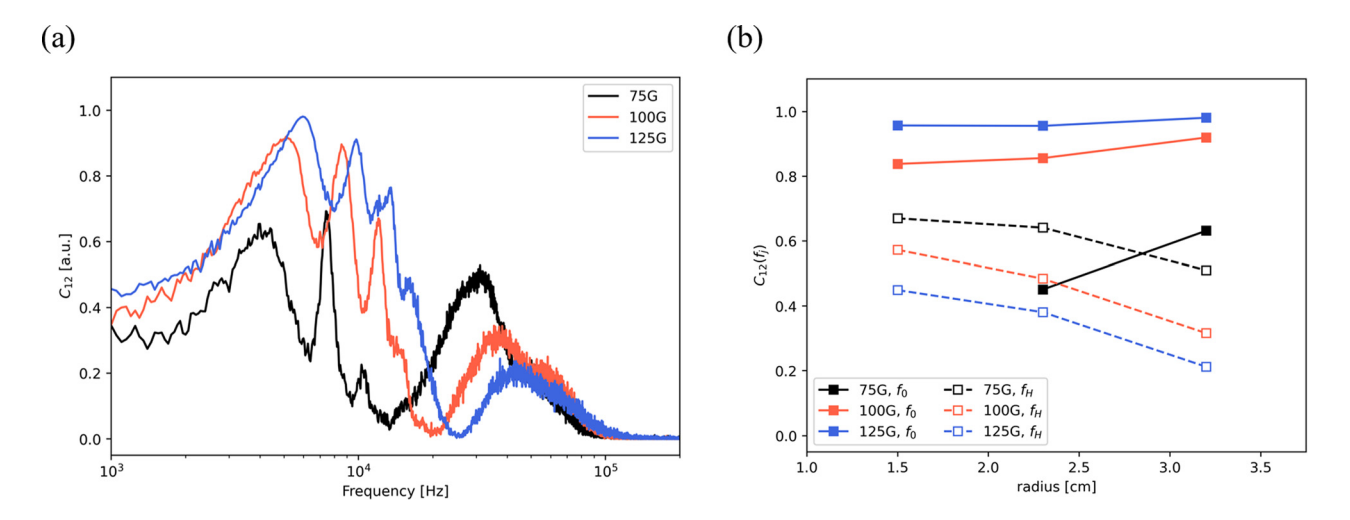


FIG. 7. (a) lon probe cross-coherence spectra measured at r=3.2 cm for several values of the applied magnetic field. (b) Mode cross coherence vs radial coordinate for the low frequency mode f_0 and high frequency mode f_H for several magnetic fields. Experimental parameters are p=0.1 mTorr, $V_c=-55$ V.

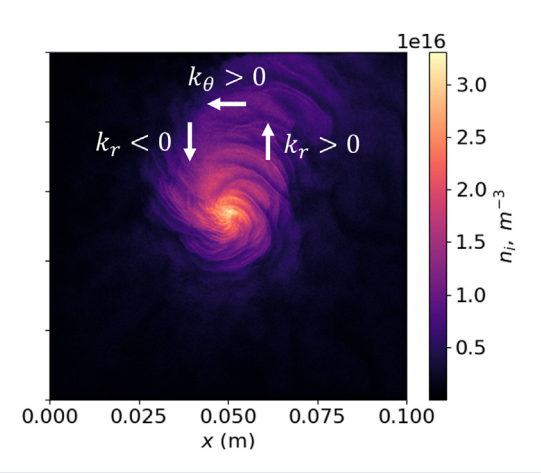


FIG. 8. Snapshot of ion density after simulation reaches saturation. Also indicated are characteristic azimuthal and radial components of the wavevector.

rotating plasma density structure is observed propagating in the $+E \times B$ direction. Furthermore, the simulation indicates that the rotating spoke is accompanied by both radially outward and inward propagating wavevectors components: ahead of the spoke, $k_r < 0$, while behind the spoke, $k_r > 0$.

A comparison of radial profiles of electron density, electron temperature, plasma potential, and azimuthal pseudospectra determined experimentally and from the PIC simulations is shown in Fig. 9. The normalized radial coordinate is defined as $\rho = r/(D_{\rm expt.}/2)$ for the experimental setup and $\rho = r/(L_{\rm x}/2)$ for the simulation setup. The time averaged electron density, electron temperature, and plasma potential radial profiles all show good agreement.

The MUSIC spectra determined by the PIC simulation reproduce the occurrence of multiple coherent azimuthal modes. However, the frequency of the azimuthal modes in the simulation is larger than in the experiment by approximately a factor of 2. This may be due to the radius of the computational domain being smaller than the experimental chamber radius by a factor of 2. Indeed, previous works have

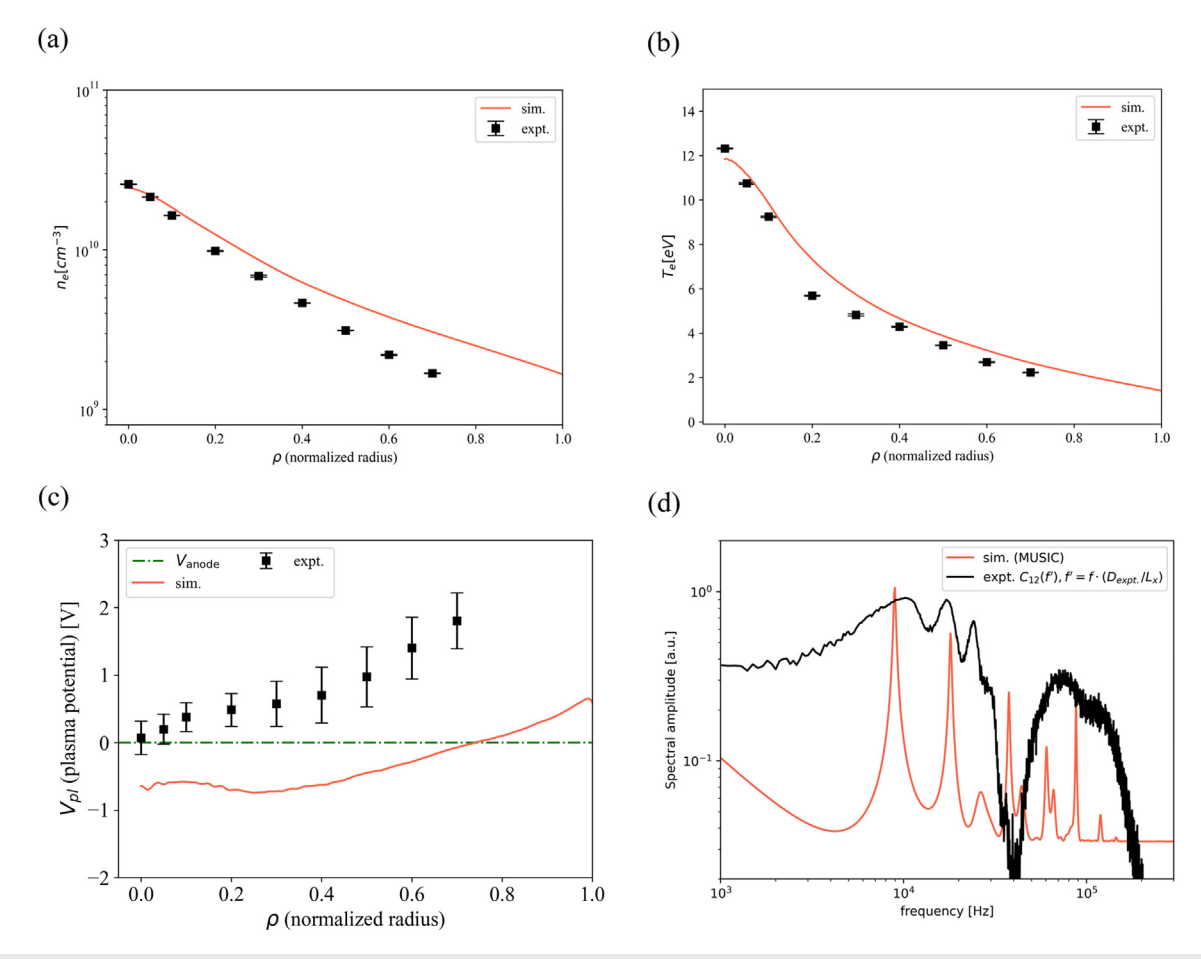


FIG. 9. Validation of radial profiles determined by experiment (expt.) and simulation (sim.) for (a) electron density n_e , (b) electron temperature T_e , and (c) plasma potential V_{pl} . Parameters are $B=100\,\mathrm{G}$, $p=0.1\,\mathrm{mTorr}$, $V_c=-55\,\mathrm{V}$. (d) Density fluctuation azimuthal pseudospectra for $\rho=0.32$ (expt.: cross-coherence C_{12} , sim.: MUSIC spectrum). The experimental cross-coherence spectrum frequency has been increased by the scaling ratio $D_{\mathrm{expt}}/L_{\mathrm{X}}=2$.

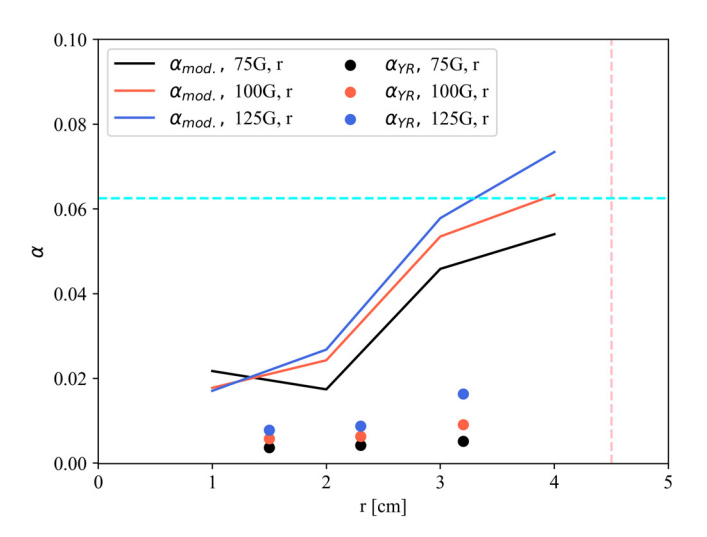


FIG. 10. Anomalous parameter $\alpha_{\rm mod.}$ as a function of radius, as determined by Eq. (13), for B=75, 100, and 125 G. Also shown is the statistically determined anomalous parameter $\alpha_{\rm YR}$. The cathode and anticathode radius $R_{\rm c,plate}=R_{atc}=4.5$ cm is indicated by the vertical dashed line, and the value of the anomalous parameter determined by Bohm is indicated by the horizontal dashed line ($\alpha=1/16$, Ref. 40).

demonstrated that increasing computational domain size reduces the frequency of azimuthal oscillations in e-beam generated $E \times B$ plasmas.²³

Quantitative agreement in the mode peak frequencies is observed between the simulated MUSIC spectrum and the experimentally determined cross-coherence when the frequency transformation $f_{\rm expt.} = f_{\rm sim.} \cdot (D_{\rm expt.}/L_x) = 2f_{\rm sim.}$ is applied to the experimental cross-coherence. This speculation should be further investigated by performing PIC simulations with a computational domain radius equal to the experimental chamber radius.

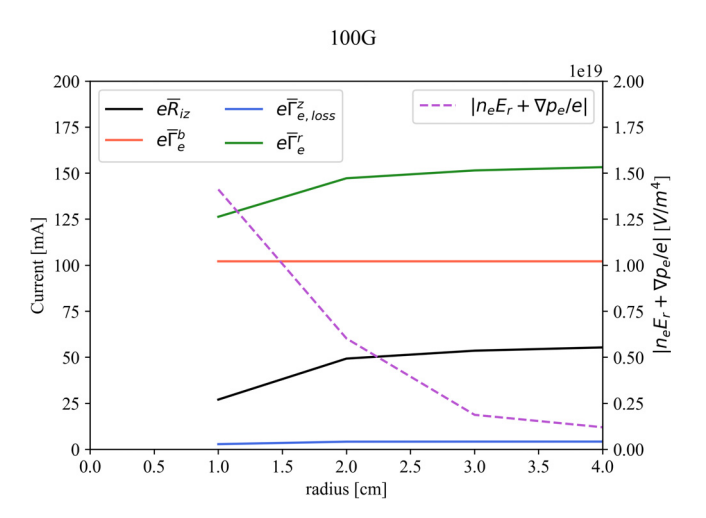


FIG. 11. Radial dependence of electron current terms and denominator from Eq. (7), for the case B = 100 G.

V. DISCUSSIONS

A. Radial electron and ion transport

Here we apply a one-dimensional model to determine the cross field anomalous electron transport in the radial direction, which is based on the electron continuity equation. This model is closely related to the zero-dimensional model developed in Ref. 24. Additionally, we apply a one-dimensional model of the ion continuity equation to determine the radial outflow velocity of ions, which is used further in Sec. V B to determine the onset of the modified Simon–Hoh instability. The electron and ion continuity equations are given by

$$\nabla \cdot \Gamma_e = R_{iz}, \tag{4}$$

$$\nabla \cdot \mathbf{\Gamma}_i = R_{iz},\tag{5}$$

where Γ_e and Γ_i are the local electron and ion fluxes, respectively, and R_{iz} is the volumetric ionization rate given by

$$R_{iz} = n_g \left(\frac{2}{m_e}\right)^{1/2} \int_0^\infty d\varepsilon \, \sigma_{iz}(\varepsilon) \varepsilon^{\frac{1}{2}} f_e(\varepsilon), \tag{6}$$

with the gas density $n_g = p/kT_g$ and neutral gas temperature assumed to be $T_g = 300$ K. Integrating Eqs. (4) and (5) over a cylindrical control volume of length L_{ch} and radius r, and solving for the radial flux, we find

$$\bar{\Gamma}_{e}^{r}(\alpha) = \bar{\Gamma}_{e}^{b} + \bar{R}_{iz} - \bar{\Gamma}_{e,loss}^{z}, \tag{7}$$

$$\bar{\Gamma}_{i}^{r} = \bar{R}_{iz} - \bar{\Gamma}_{i}^{z}, \tag{8}$$

where $\bar{\Gamma}_{e,loss}^z$, $\bar{\Gamma}_e^r(\alpha)$, $\bar{\Gamma}_e^b$, $\bar{\Gamma}_i^z$, and $\bar{\Gamma}_i^r$ are the surface integrated axial electron loss flux, radial electron flux, injected electron beam flux, axial ion flux, and radial ion flux, respectively, and \bar{R}_{iz} is the volume integrated ionization rate. The semi-empirically determined anomalous parameter α is the inverse Hall parameter. The quantities expressed in Eqs. (7) and (8) are explicitly defined as

$$\bar{\Gamma}_{e,\text{loss}}^{z} = 2\pi \int_{0}^{r} r' dr' \frac{n_{e} v_{the}}{4} \times \left\{ \exp\left(-\frac{(V_{pl} - V_{c})}{kT_{e}}\right) + \min\left[\exp\left(-\frac{(V_{pl} - V_{atc})}{kT_{e}}\right), 1\right] \right\},$$
(9)

$$\bar{\Gamma}_{e}^{r}(\alpha) = -\mu_{e\perp}(\alpha) \left(n_{e} E_{r} + \frac{\nabla p_{e}}{e} \right) \cdot (2\pi L_{ch} r), \tag{10}$$

$$\bar{R}_{iz}(r) = 2\pi L_{ch} \int_0^r r' dr' R_{iz},$$
 (11)

$$\bar{\Gamma}_{i}^{z} = 2 \times 2\pi \int_{0}^{r} r' dr' (0.61 n_{e} \nu_{\text{Bohm}}),$$
 (12)

and the injected electron beam flux is approximately the discharge current $\bar{\Gamma}_e^b \approx I_d/e$. Here, we make the approximations that the net axial flux of electrons is given by the electron thermal flux confined by the cathode and anticathode sheaths. We also assume axial uniformity, that the radial electron flux is given by the drift-diffusion approximation, and that the EEDF is isotropic. Furthermore, we assume the cathode and anticathode sheaths are planar and therefore approximate the axial ion flux as the Bohm current, with the sheath density $n_s = 0.61 \, n_e$ and ion velocity entering the sheath as $\nu_{\rm Bohm} = \left(k_B T_e/m_{\rm Ar}\right)^{0.5}$ where $m_{\rm Ar}$ is the mass of an Argon ion.

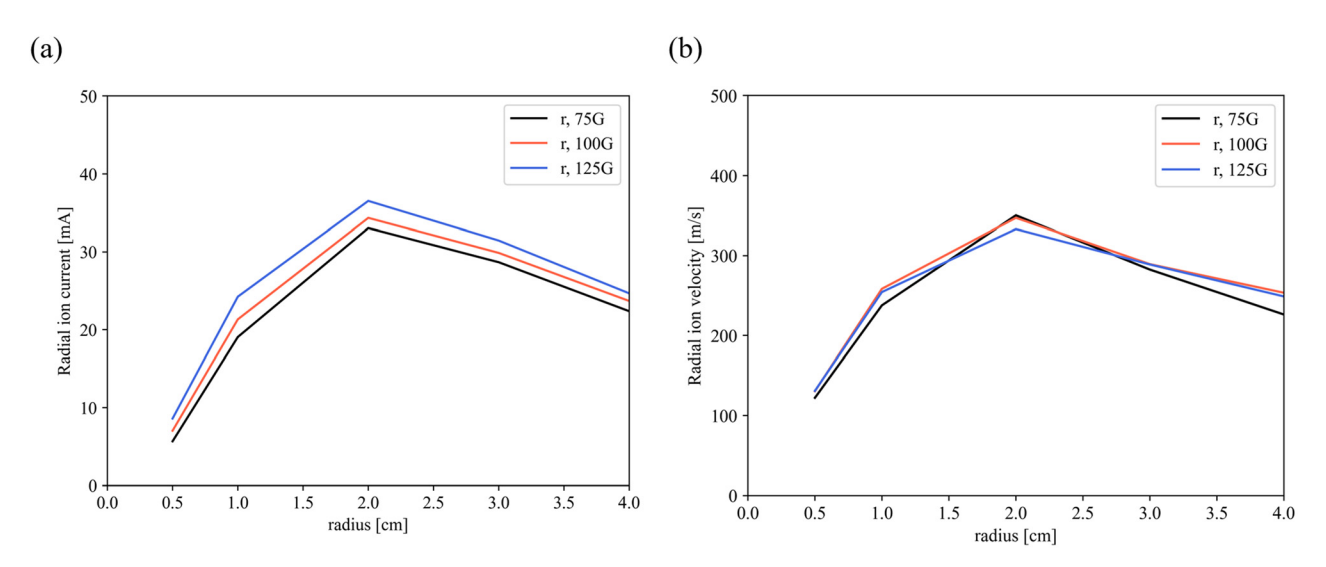


FIG. 12. Radial dependence of (a) ion current e $\bar{\Gamma}_i^r$ and (b) radial ion velocity determined by ion current continuity, for magnetic fields B=75, 100, and 125 G.

The prefactor of 2 occurring in Eq. (12) accounts for the Bohm ion current collected by both the anticathode and cathode surfaces. Finally, we neglect the Simon effect for electrons "short circuiting" across the magnetic field lines through the axial conducting boundaries. ^{35,36} We make this assumption since the discharge is operated in the repeller mode, in which case both anticathode and cathode have a large electron reflecting sheath. Under such conditions, a negligible electron flux will strike either conducting boundary.

In a previous work on a similar e-beam generated $E \times B$ plasma, it was determined that electron–neutral collisions are insufficient to explain the electron cross field transport, and electron transport rather is so-called "anomalous," i.e., driven by effective electron collisions with fluctuations in the plasma. ²⁴ In the case of anomalous cross field

electron transport such that $\nu_{en} \ll \alpha \omega_{ce}$, the electron cross field mobility can be approximated as $\mu_{e\perp}(\alpha) \approx \alpha/B$. $^{37-39}$ Under such conditions, Eq. (7) can be solved for the anomalous parameter,

$$\alpha(r) = \frac{\bar{\Gamma}_e^b + \bar{R}_{iz} - \bar{\Gamma}_{e,loss}^z}{-\frac{1}{B} \left(n_e E_r + \frac{\nabla p_e}{e} \right) 2\pi r L_{ch}}.$$
 (13)

The anomalous parameter α as a function of the radial coordinate is shown for several values of the applied magnetic field in Fig. 10. The statistically determined anomalous parameter using the mean-squared ion density fluctuation determined from IP1, $\alpha_{YR} = 0.25 \pi (n - n_0)^2/n_0^2$, as derived by Ref. 37, is also shown.

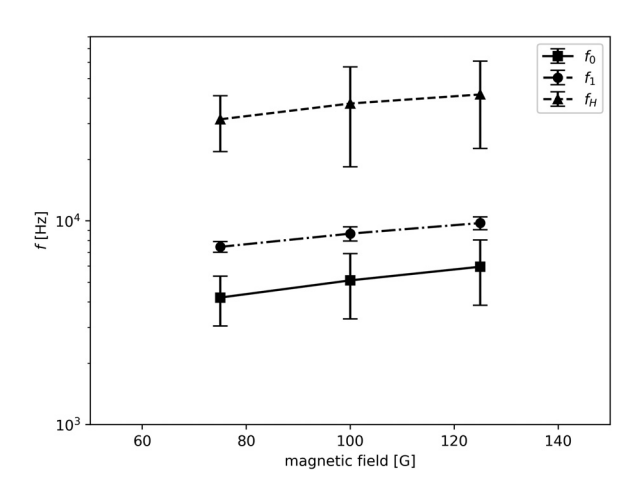


FIG. 13. Frequency of f_0 , f_1 , and f_H modes at radial position r=3.2 cm, as a function of applied magnetic field. Error bars in the mode frequency are given from the FWHM of the peaks in the cross-coherence spectrum. Experimental parameters are $\rho=0.1\,\mathrm{mTorr}$, $V_c=-55\,\mathrm{V}$.

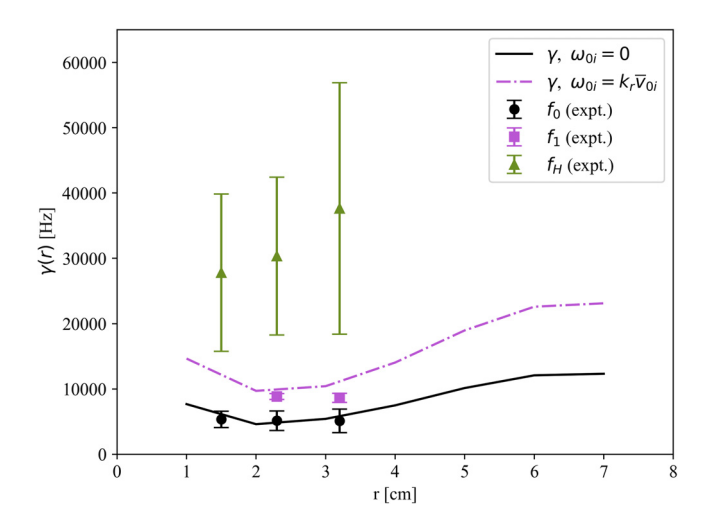


FIG. 14. MSHI growth rate assuming $\omega_{0i}=0$, $\omega_{0i}=k_r \bar{\nu}_{0i}$. Also shown are the experimentally determined f_0 , f_1 , and f_H mode dependence on radius as determined by the azimuthal ion probe array. Experimental parameters are $B=100\,\mathrm{G}$, $p=0.1\,\mathrm{mTorr}$, $V_c=-55\,\mathrm{V}$.

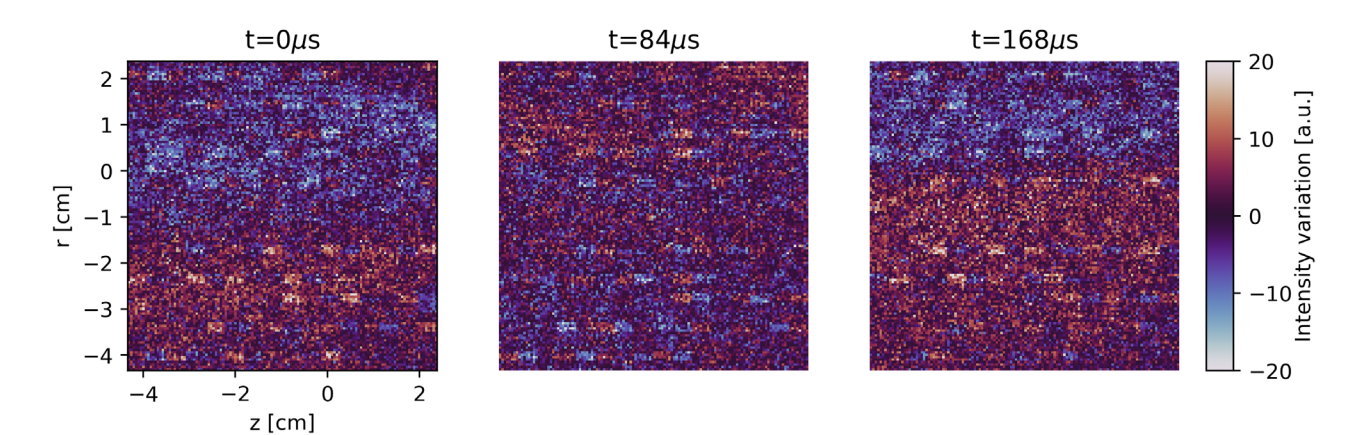


FIG. 15. Mean subtracted fast frame image sequence of one cycle of the 6 kHz mode. Images are in the r-z plane, with radial coordinate on the vertical axis and axial coordinate on the horizontal axis. The red region indicates an optically brighter region of the plasma, while the blue region indicates optically dimmer, as compared to the time averaged brightness of the fast frame sequence. Experimental parameters are $B=100\,\mathrm{G},\,V_c=-55\,\mathrm{V}.$

Both the model based on Eq. (13) and the statistically determined α_{YR} agree in the trend of relatively low value of the anomalous transport factor in the region $r \leq 2$ cm, with sharply increasing anomality for r > 2 cm. Additionally, both $\alpha_{\text{mod.}}$ and α_{YR} tend to increase with increasing magnetic field, indicating higher cross field electron transport at larger magnetic fields. This trend predicted by the model agrees with the observation of enhanced mode coherence at larger magnetic field observed from the azimuthal ion probe measurements (Fig. 7). Therefore, the enhancement of anomalous transport in the r > 2 cm is likely due to the enhancement of the spoke.

The modeled anomalous parameter is reduced significantly by at least a factor of 2 at r=1.5 cm compared to r=3.2 cm. This is caused by the enhanced ionization rate near the discharge center for $r \leq 2$ cm. For r > 2 cm, ionization is not sufficient to sustain the electron transport, and therefore the anomalous factor increases to maintain the electron continuity.

To explain the radial dependence of the anomalous transport, the radial dependence of the electron current terms from Eq. (7) are shown in Fig. 11 in the case B=100 G. For $r\geq 2$ cm the electron current due to ionization $e\bar{R}_{iz}$ saturates. However, the absolute value of the gradient terms in the denominator of Eq. (7) continue to reduce for $r\geq 2$ cm. The dominant term in the denominator is the electron pressure gradient ∇p_e , which indeed shows a sharp decline in magnitude for r>2 cm (Subsection 2 of the Appendix, Fig. 21). Therefore, an enhancement in α for $r\geq 2$ cm occurs to compensate for the reduction in the electron pressure gradient, so that the radial electron current $e\bar{\Gamma}^p_e$ can balance the injected beam current $e\bar{\Gamma}^b_e$.

Using the experimentally determined radial profiles for the electron density, electron temperature, and ionization rate (Subsection 2 of the Appendix), the radial ion current can be determined by solving Eqs. (8), (11), and (12) for $e\bar{\Gamma}_i^r$,

$$e\bar{\Gamma}_{i}^{r} = 2\pi L_{ch} \int_{0}^{r} r' dr' R_{iz} - 2 \times 2\pi \int_{0}^{r} r' dr' (0.61 n_{e} \nu_{\text{Bohm}}).$$
 (14)

Additionally, the radial outward ion velocity can be computed as

$$\bar{\nu}_{0i} = \bar{\Gamma}_i^r / 2\pi r L_{ch}. \tag{15}$$

The resulting values of $e\overline{\Gamma}_i^r$ and $\overline{\nu}_{0i}$ are shown in Fig. 12. Evidently a radially outward ion current is necessary to satisfy global ion current continuity, generating an ion flow velocity that reaches approximately $\overline{\nu}_{0i}=350$ m/s in the radial outward direction. For r>2 cm, the radial ion current and resulting radial ion velocity reduce. This occurs since the volume integrated ionization rate saturates for $r\geq 2$ cm [Subsection 2 of the Appendix, Fig. 19(a)], while the surface integrated Bohm ion current as determined by Eq. (12) leaving the cylindrical endcaps to either cathode and anticathode continues to increase linearly (Subsection 2 of the Appendix, Fig. 20). This steady state radial outflow of ions has been predicted in previous works of similar e-beam generated $E\times B$ plasmas. Doppler shift laser induced fluorescence (LIF) measurements are currently being conducted to directly measure the ion flow in the plasma and will be reported in a separate paper.

B. Physical origins of multimodal azimuthal oscillations

The magnetic field scaling of the experimentally observed azimuthal modes are shown in Fig. 13. Moreover, the f_0 mode is amplified at larger radii $r \geq 2$ cm, while the f_H mode decays at larger radii. The trend of increasing azimuthal modes frequency with increasing magnetic field is consistent with previous studies on similar $E \times B$ devices. 12,13,23

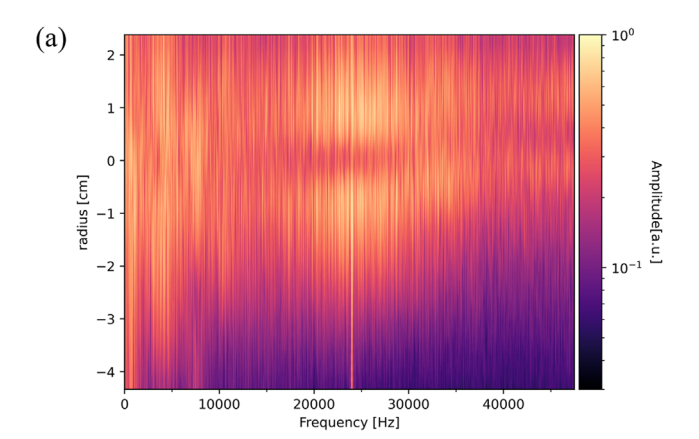
The modified Simon–Hoh dispersion relation derived from the linearized fluid equations is given as 43

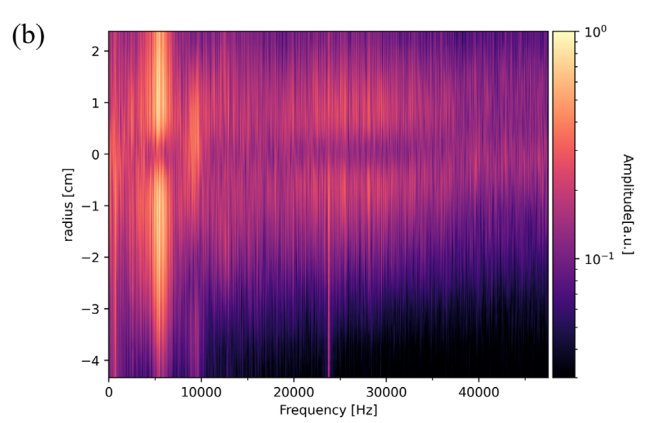
$$\omega = \omega_{0i} + \frac{k^2 c_s^2}{2\omega_*} + \sqrt{\frac{k^4 c_s^4}{4\omega_*^2} + \frac{k^2 c_s^2}{\omega_*} (\omega_{0i} - \omega_0)},$$
 (16)

where $k = (k_r^2 + k_\theta^2)^{1/2}$ is the wavevector amplitude, $c_s = (k_B T_e/m_{Ar})^{0.5}$ is the bulk ion sound speed, $\omega_{0i} = \mathbf{k} \cdot \mathbf{v}_{0i}$ is the ion response frequency corresponding to ion flow with velocity \mathbf{v}_{0i} , $\omega_0 = -k_\theta E_r/B$ is the electron $\mathbf{E} \times \mathbf{B}$ frequency, and $\omega_* = -k_\theta k_B T_e/eBL_n$ is the electron diamagnetic drift frequency with radial gradient length scale defined as $L_n \equiv n_e (\partial n_e/\partial r)^{-1}$. Instability occurs for $\gamma \equiv \mathrm{Im}(\omega) > 0$. Importantly, electron $\mathbf{E} \times \mathbf{B}$ flow is always destabilizing, while the ion

response is destabilizing when there is ion flow counterpropagating with the wavevector, i.e., $k\cdot v_{0i}<0.$

There are several mechanisms in which ion flow can contribute to the MSHI growth rate. ¹³ Here we consider the effect of the radially outward directed equilibrium ion flow velocity estimated from the ion continuity Eq. (15), $\bar{v}_{0i} > 0$. This ion flow is destabilizing for the case $k_r < 0$. Indeed, the PIC simulations indicate the existence of a spatially





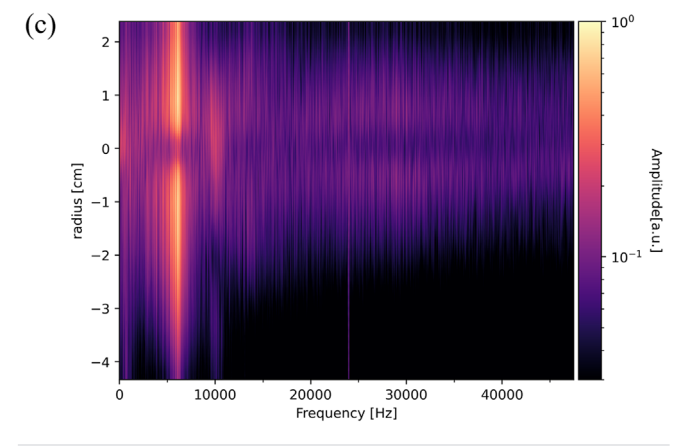


FIG. 16. Spectrograms of the axially averaged fast frame sequence taken at 95 kfps for magnetic field (a) $B=75\,\mathrm{G}$, (b) $B=100\,\mathrm{G}$, and (c) $B=125\,\mathrm{G}$. Experimental parameters are $p=0.1\,\mathrm{mTorr}$, $V_c=-55\,\mathrm{V}$.

dependent wavevector $\mathbf{k} = k_r \hat{\mathbf{r}} + k_\theta \hat{\theta}$, with k_r taking both positive and negative values (Fig. 8). Therefore, these different processes associated with the ion flow may further destabilize the drift wave associated with Simon–Hoh Instability onset.

Using experimental radial profiles for the electron density [Fig. 18(a)], electron temperature [Fig. 18(b)], and plasma potential [Fig. 19(b)], we determine radial profiles of γ for the cases with and without ion responses. Here we assume a single-lobed (m=1) spoke centered at $R_{c,\text{plate}}/2$, such that the azimuthal wavenumber is $k_\theta = 2/R_{c,\text{plate}}$. Furthermore, in the cases where nonzero ion response is considered, the radial wavenumber is assumed to be single lobed in the radial direction, such that $k_r = \pi/R_{c,\text{plate}}$. However, as supported by the simulations (Fig. 8), fine structures in the plasma density may form in the radial direction, indicating that the radial wavenumber may be significantly larger than considered here.

The calculated MSHI growth rate γ radial profiles are shown in Fig. 14, considering the cases of no ion response and bulk ion velocity outward \bar{v}_{0i} , as calculated by Eq. (15). Evidently, γ shows good agreement with the f_0 and f_1 modes under the assumption of no ion response and outward ion flow, respectively.

This suggests future experimental studies and simulations should be carried out to precisely determine the ion dynamics and their role in the spoke formation in e-beam generated $E \times B$ plasmas, for instance, using Doppler shift LIF. MSHI theory as described by Eq. (16) does not predict the formation of harmonics or multiple simultaneous modes. We would also like to emphasize that the MSHI dispersion relation is based on linear theory and may not capture the full set of nonlinear or nonlocal physical mechanisms occurring in the saturated state of the spoke. ^{19,43,46} Furthermore, while this work has focused on oscillations in the $r-\theta$ plane, the e-beam generated $E \times B$ plasma considered here is inherently three-dimensional. Axial variations in plasma density and electric field may influence the azimuthal mode formation. Indeed, recent simulations have demonstrated the formation of helical structures in e-beam generated $E \times B$ plasmas. ⁴⁷

VI. CONCLUSION

In this work, we investigated the radial dependence of azimuthally propagating plasma oscillations in an electron beam generated $E \times B$ plasma operated with an electron repelling anticathode. Experimental ion probe and fast frame imaging measurements indicate that at least three distinct azimuthal modes (with oscillation frequencies f_0 , f_1 , and f_H) simultaneously occur in the 5–50 kHz frequency band. Furthermore, the f_0 and f_H modes exhibit a single-lobed (m=1) azimuthal mode number. These modes exhibit a complex radial dependence, with the lower frequency (f_0) mode dominant in the plasma periphery and the higher frequency (f_H) mode more dominant near the plasma center.

The experimental measurements are corroborated with a 2D3V PIC simulation, which is experimentally validated in this work and shows good agreement with time averaged radial plasma density, electron temperature, and plasma potential profiles. The azimuthal mode spectrum observed in the PIC simulation corroborates the azimuthal mode spectrum determined experimentally with the ion probe array.

The radial dependence of the anticathode bias on the azimuthal oscillations is analyzed using a 1D electron continuity model. The model indicates that there is enhanced anomalous transport in the peripheral plasma region, which coincides with the growth of the additional azimuthal modes in this region. Furthermore, it is suggested that

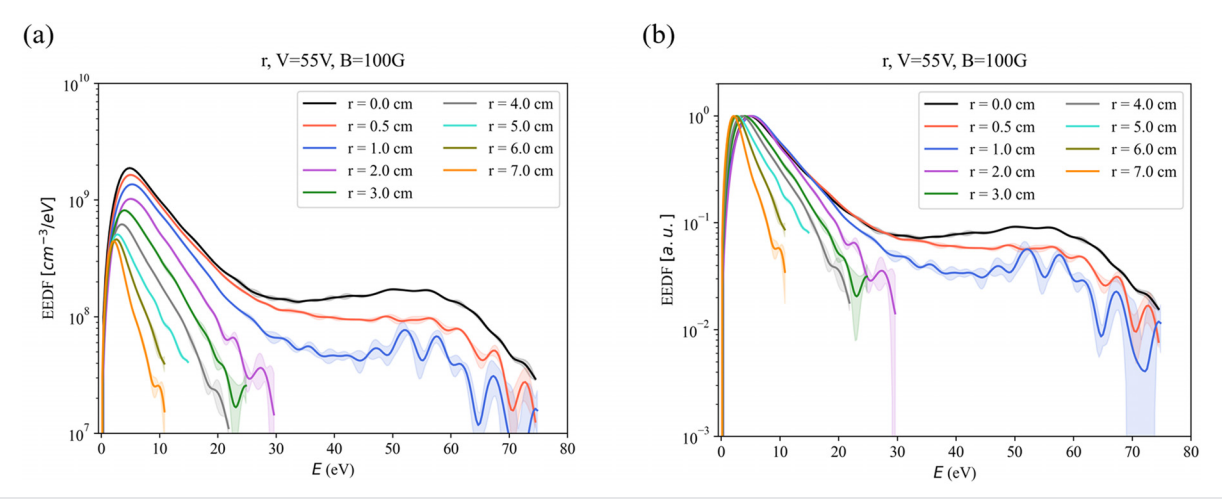


FIG. 17. EEDF determined by LP at $B=100\,\mathrm{G},\,V_c=-55\,\mathrm{V},\,p=0.1\,\mathrm{mTorr},\,\mathrm{for}$ (a) in absolute units and (b) normalized to EEDF maximum.

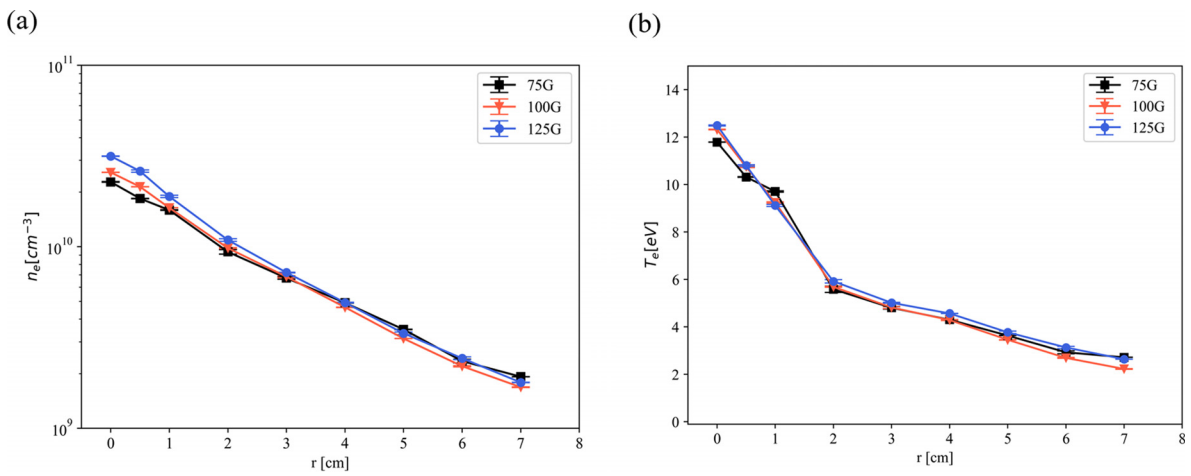


FIG. 18. Radial profile of (a) plasma density $n_{\rm e}$ determined by LP and (b) electron temperature $T_{\rm e}$ for varying magnetic field, $V_c=-55\,{\rm V}$, $p=0.1\,{\rm mTorr}$.

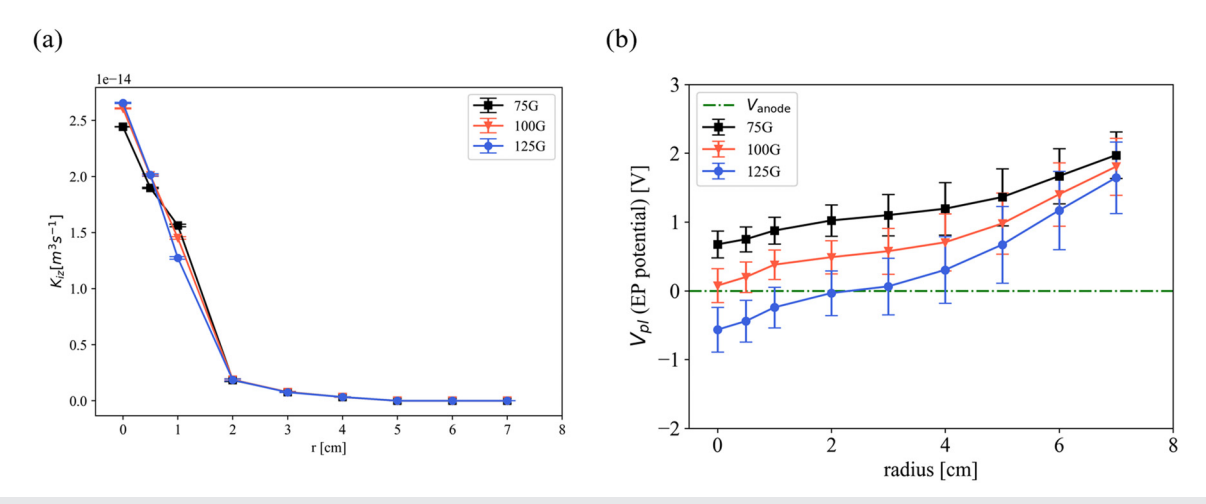


FIG. 19. (a) Ionization rate constant K_{iz} radial profile determined by LP and (b) plasma potential V_{pl} radial profile determined by EP for varying magnetic field, $V_c = -55 \, \text{V}$, $\rho = 0.1 \, \text{mTorr}$.

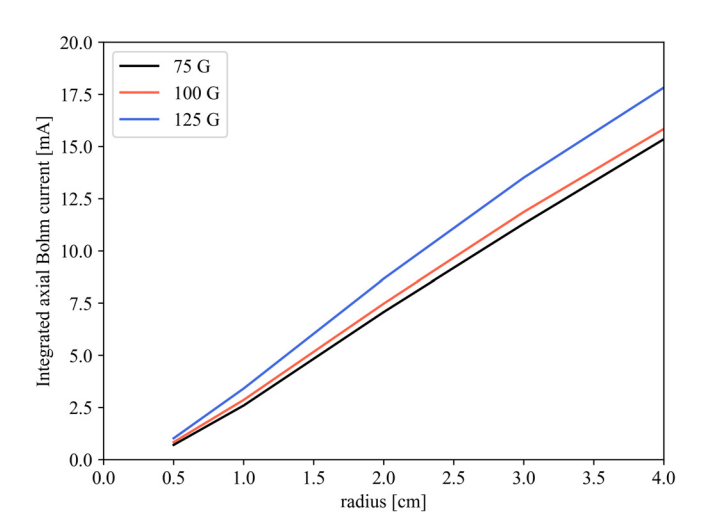


FIG. 20. Surface integrated Bohm ion current as determined by Eq. (14), for varying magnetic field and parameters $V_c = -55 \, \text{V}$, $p = 0.1 \, \text{mTorr}$.

the suppression of anomalous transport in the central plasma region is caused by a balance of fluxes driven by ionization and electron pressure.

The physical mechanisms leading to the azimuthal mode spectrum are further analyzed by applying the linear theory of MSHI, making consideration of some possible mechanisms by which ion dynamics can affect the instability onset. We find that the lowest frequency (f_0) m=1 azimuthal mode is closely predicted by the MSHI dispersion relation by neglecting ion dynamics. By considering the radial outflow of ions calculated from solving the ion continuity, we find that the harmonic (f_1) mode may be predicted by MSHI with reasonable agreement. However, the finding of multiple simultaneously occurring azimuthal modes is not predicted by MSHI with a simple equilibrium ion flow. Furthermore, even with the effect of radial ion

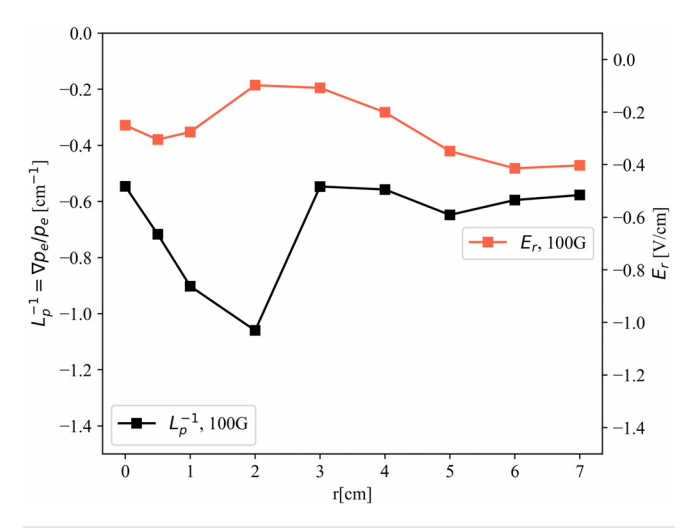


FIG. 21. Radial profiles of electron pressure gradient inverse length scale L_p^{-1} and radial electric field for. $B=100~{\rm G},~V_c=-55~{\rm V},~p=0.1~{\rm mTorr}.$

flow taken into account, MSHI significantly underpredicts the higher frequency (f_H) mode. Future studies should be conducted to investigate the relationship between azimuthal mode formation and resulting ion kinetics, potentially allowing the development of e-beam E \times B plasmas with low ion energies in the peripheral plasma region that are more suited for material processing applications.

ACKNOWLEDGMENTS

This research was supported by the U.S. Department of Energy, Office of Fusion Energy Science, under Contract No. DEAC02-09CH11466, as a part of the Princeton Collaborative Low Temperature Plasma Research Facility (PCRF). The authors are grateful to Ivan Romadanov and Sunghyun Son for fruitful discussions regarding the physics of electron beam generated $E\times B$ plasmas and cross field transport, and Timothy K. Bennett for technical support on the electron beam chamber.

AUTHOR DECLARATIONS Conflict of Interest

The authors have no conflicts to disclose.

Author Contributions

Nirbhav Singh Chopra: Conceptualization (equal); Data curation (equal); Formal analysis (equal); Investigation (equal); Methodology (equal); Validation (equal); Writing – original draft (equal). Mina Papahn Zadeh: Investigation (equal); Methodology (equal); Software (equal); Writing – review & editing (equal). Mikhail Tyushev: Conceptualization (equal); Methodology (equal); Software (equal); Writing – review & editing (equal). Andrei Smolyakov: Conceptualization (equal); Software (equal); Supervision (equal); Writing – review & editing (equal). Alexandre Likhanskii: Conceptualization (equal); Software (equal); Writing – review & editing (equal). Yevgeny Raitses: Conceptualization (equal); Funding acquisition (equal); Investigation (equal); Methodology (equal); Supervision (equal); Writing – review & editing (equal).

DATA AVAILABILITY

The data that support the findings of this study are available from the corresponding author upon reasonable request.

APPENDIX: FAST FRAME IMAGING, EEDFS, AND MACROSCOPIC PLASMA PARAMETERS

1. Fast frame imaging corroboration of azimuthal plasma oscillations

An example fast frame image sequence of the optical plasma emission in the r-z plane of the plasma is shown in Fig. 15.

The fast frame image sequences were collected for varying magnetic field B=75, 100, and 125 G. Each frame was axially averaged, which yielded an optical intensity temporal signal $\tilde{I}(r,t)$ for each radial position r. Spectrograms consisting of the Fourier transform of $\tilde{I}(r,t)$ at each r, $F(\tilde{I})(r,f)$, are shown in Fig. 16. The fast

frame spectrograms corroborate the azimuthal probe array measurements, indicating both the presence of f_0 and f_H as azimuthally propagating modes.

2. Electron energy distribution function and macroscopic plasma parameters

The EEDFs and macroscopic parameters determine by Langmuir and emissive probes used in this work are shown in Figs. 17–19.

The surface integrated Bohm ion current leaving the cylindrical endcaps to either cathode, as determined by Eq. (12), is shown in Fig. 20.

The radial profiles of electron pressure gradient inverse length scale and radial electric field as determined by LP and EP in this work are shown in Fig. 21.

REFERENCES

- ¹F. Zhao, Y. Raitses, X. Yang, A. Tan, and C. G. Tully, "High hydrogen coverage on graphene via low temperature plasma with applied magnetic field," Carbon 177, 244–251 (2021).
- ²S. G. Walton, D. R. Boris, S. C. Hernández, E. H. Lock, Tz. B. Petrova, G. M. Petrov, and R. F. Fernsler, "Electron beam generated plasmas for ultra low T_e processing," ECS J. Solid State Sci. Technol. 4(6), N5033–N5040 (2015).
- ³D. B. Zolotukhin, V. A. Burdovitsin, and E. M. Oks, "On the role of secondary electrons in beam plasma generation inside a dielectric flask by fore-vacuum plasma-cathode electron source," Phys. Plasmas 24(9), 093502 (2017).
- ⁴K. D. Schatz and D. N. Ruzic, "An electron-beam plasma source and geometry for plasma processing," Plasma Sources Sci. Technol. 2(2), 100–105 (1993).
- ⁵S. Rauf, A. Balakrishna, A. Agarwal, L. Dorf, K. Collins, D. R. Boris, and S. G. Walton, "Three-dimensional model of electron beam generated plasma," Plasma Sources Sci. Technol. **26**(6), 065006 (2017).
- ⁶S. Rauf, D. Sydorenko, S. Jubin, W. Villafana, S. Ethier, A. Khrabrov, and I. Kaganovich, "Particle-in-cell modeling of electron beam generated plasma," Plasma Sources Sci. Technol. 32(5), 055009 (2023).
- ⁷D. R. Boris, G. M. Petrov, E. H. Lock, T. B. Petrova, R. F. Fernsler, and S. G. Walton, "Controlling the electron energy distribution function of electron beam generated plasmas with molecular gas concentration: I. Experimental results," Plasma Sources Sci. Technol. 22(6), 065004 (2013).
- ⁸R. F. Fernsler, W. M. Manheimer, R. A. Meger, J. Mathew, D. P. Murphy, R. E. Pechacek, and J. A. Gregor, "Production of large-area plasmas by electron beams," Phys. Plasmas 5(5), 2137–2143 (1998).
- ⁹W. M. Manheimer, R. F. Fernsler, M. Lampe, and R. A. Meger, "Theoretical overview of the large-area plasma processing system (LAPPS)," Plasma Sources Sci. Technol. 9, 370–386 (2000).
- ¹⁰S. Yatom, N. Chopra, S. Kondeti, T. B. Petrova, Y. Raitses, D. R. Boris, M. J. Johnson, and S. G. Walton, "Measurement and reduction of Ar metastable densities by nitrogen admixing in electron beam-generated plasmas," Plasma Sources Sci. Technol. 32(11), 115005 (2023).
- ¹¹L. Dorf, J.-C. Wang, S. Rauf, Y. Zhang, A. Agarwal, J. Kenney, K. Ramaswamy, and K. Collins, "Atomic precision etch using a low-electron temperature plasma," Proc. SPIE 9782, 97820J (2016).
 ¹²E. Rodríguez, V. Skoutnev, Y. Raitses, A. Powis, I. Kaganovich, and A.
- ¹²E. Rodríguez, V. Skoutnev, Y. Raitses, A. Powis, I. Kaganovich, and A. Smolyakov, "Boundary-induced effect on the spoke-like activity in $E \times B$ plasma," Phys. Plasmas **26**(5), 053503 (2019).
- ¹³Y. Sakawa, C. Joshi, P. K. Kaw, F. F. Chen, and V. K. Jain, "Excitation of the modified Simon–Hoh instability in an electron beam produced plasma," Phys. Fluids B 5(6), 1681–1694 (1993).
- ¹⁴M. Farley, P. Rose, and G. Ryding, "Freeman and bernas ion sources," in *The Physics and Technology of Ion Sources*, edited by I. G. Brown (Wiley-VCH Verlag GmbH & Co. KGaA, Weinheim, 2005), pp. 133–161.
- 15 F. F. Chen, "Radial electric field in a reflex discharge," Phys. Rev. Lett. 8(6), 234–237 (1962).

- ¹⁶J. P. Boeuf and M. Takahashi, "New insights into the physics of rotating spokes in partially magnetized E × B plasmas," Phys. Plasmas 27(8), 083520 (2020).
- 17 J. W. Koo and I. D. Boyd, "Modeling of anomalous electron mobility in Hall thrusters," Phys. Plasmas 13(3), 033501 (2006).
- ¹⁸M. Lee, K.-J. Chung, K. Hara, and J. Y. Kim, "Discharge mode transition in partially magnetized E × B Penning discharge," Phys. Plasmas 31(12), 123508 (2024).
- ¹⁹O. Koshkarov, A. Smolyakov, Y. Raitses, and I. Kaganovich, "Self-organization, structures, and anomalous transport in turbulent partially magnetized plasmas with crossed electric and magnetic fields," Phys. Rev. Lett. 122(18), 185001 (2019).
- ²⁰K. Hara, A. R. Mansour, and S. Tsikata, "Theory of gradient drift instabilities in low-temperature, partially magnetised plasmas," J. Plasma Phys. 88(4), 905880408 (2022).
- ²¹Y.-Q. Tao, R. W. Conn, L. Schmitz, and G. Tynan, "Collisionless Simon-Hoh instability in a strongly double-sheared electric field," Phys. Plasmas 1(10), 3193–3198 (1994).
- ²²A. Likhanskii, A. Smolyakov, M. Papahn Zadeh, N. Chopra, and Y. Raitses, "3D effects in the simulations of the magnetized DC plasma sources for ion implantation," in APS Gaseous Electronics Conference, 2023.
- ²³ M. Tyushev, M. Papahn Zadeh, V. Sharma, M. Sengupta, Y. Raitses, J.-P. Boeuf, and A. Smolyakov, "Azimuthal structures and turbulent transport in Penning discharge," Phys. Plasmas 30(3), 033506 (2023).
- ²⁴N. S. Chopra, I. Romadanov, and Y. Raitses, "Anticathode effect on electron kinetics in electron beam generated E × B plasma," Plasma Sources Sci. Technol. 33(12), 125003 (2024).
- 25Y. Raitses, D. Staack, A. Smirnov, and N. J. Fisch, "Space charge saturated sheath regime and electron temperature saturation in Hall thrusters," Phys. Plasmas 12(7), 073507 (2005).
- ²⁶H. M. Mott-Smith and I. Langmuir, "The theory of collectors in gaseous discharges," Phys. Rev. 28(4), 727–763 (1926).
- ²⁷P. Welch, "The use of fast Fourier transform for the estimation of power spectra: A method based on time averaging over short, modified periodograms," IEEE Trans. Audio Electroacoust. 15(2), 70–73 (1967).
- ²⁸L. B. White and B. Boashash, "Cross spectral analysis of nonstationary processes," IEEE Trans. Inform. Theory 36(4), 830–835 (1990).
- 29 L. Fedeli, A. Huebl, F. Boillod-Cerneux, T. Clark, K. Gott, C. Hillairet, S. Jaure, A. Leblanc, R. Lehe, A. Myers, C. Piechurski, M. Sato, N. Zaim, W. Zhang, J.-L. Vay, and H. Vincenti, "Pushing the Frontier in the design of laser-based electron accelerators with groundbreaking mesh-refined particle-in-cell simulations on exascale-class supercomputers," in SC22: International Conference for High Performance Computing, Networking, Storage and Analysis (IEEE, Dallas, TX, 2022).
- ³⁰M. Tyushev, M. Papahn Zadeh, N. S. Chopra, Y. Raitses, I. Romadanov, A. Likhanskii, G. Fubiani, L. Garrigues, R. Groenewald, and A. Smolyakov, "Mode transitions and spoke structures in $E \times B$ Penning discharge," Phys. Plasmas **32**(1), 013511 (2025).
- ³¹L. C. Pitchford, L. L. Alves, K. Bartschat, S. F. Biagi, M. C. Bordage, A. V. Phelps, C. M. Ferreira, G. J. M. Hagelaar, W. L. Morgan, S. Pancheshnyi, V. Puech, A. Stauffer, and O. Zatsarinny, "Comparisons of sets of electron-neutral scattering cross sections and swarm parameters in noble gases: I. Argon," J. Phys. D 46(33), 334001 (2013).
- ³²C. Yamabe, S. J. Buckman, and A. V. Phelps, "Measurement of free-free emission from low-energy-electron collisions with Ar," Phys. Rev. A 27(3), 1345–1352 (1983).
- ³³O. Zatsarinny and K. Bartschat, "B-spline Breit-Pauli R-matrix calculations for electron collisions with argon atoms," J. Phys. B 37(23), 4693–4706 (2004).
- ³⁴L. Xu, D. Eremin, and R. P. Brinkmann, "Direct evidence of gradient drift instability being the origin of a rotating spoke in a crossed field plasma," Plasma Sources Sci. Technol. 30(7), 075013 (2021).
- 35A. Simon, "Ambipolar diffusion in a magnetic field," Phys. Rev. 98(2), 317–318 (1955).
- ³⁶D. Curreli and F. F. Chen, "Cross-field diffusion in low-temperature plasma discharges of finite length," Plasma Sources Sci. Technol. 23(6), 064001 (2014).
- ³⁷S. Yoshikawa and D. J. Rose, "Anomalous diffusion of a plasma across a magnetic field," Phys. Fluids 5(3), 334–340 (1962).
- ³⁸J. P. Boeuf and L. Garrigues, "Low frequency oscillations in a stationary plasma thruster," J. Appl. Phys. 84(7), 3541–3554 (1998).

- ³⁹J. Bareilles, G. J. M. Hagelaar, L. Garrigues, C. Boniface, J. P. Boeuf, and N. Gascon, "Critical assessment of a two-dimensional hybrid Hall thruster model: Comparisons with experiments," Phys. Plasmas 11(6), 3035–3046 (2004).
- ⁴⁰D. Bohm, E. H. S. Burhop, and H. S. W. Massey, The Characteristics of Electrical Discharges in Magnetic Fields (McGraw-Hill, 1949).
- ⁴¹N. S. Chopra, I. Romadanov, and Y. Raitses, "Production of warm ions in electron beam generated E × B plasma," Appl. Phys. Lett. **124**, 064101 (2024).
- ⁴²S. Son, I. Romadanov, N. Chopra, and Y. Raitses, "Measurements of two-dimensional ion velocity distributions in electron beam generated E × B plasma," in APS Division of Plasma Physics, Atlanta, GA, 2024.
- plasma," in APS Division of Plasma Physics, Atlanta, GA, 2024.

 43A. I. Smolyakov, O. Chapurin, W. Frias, O. Koshkarov, I. Romadanov, T. Tang, M. Umansky, Y. Raitses, I. D. Kaganovich, and V. P. Lakhin, "Fluid theory and simulations of instabilities, turbulent transport and coherent structures in
- partially-magnetized plasmas of E×B discharges," Plasma Phys. Controlled Fusion **59**(1), 014041 (2017).
- ⁴⁴A. M. Keesee, E. E. Scime, and R. F. Boivin, "Laser-induced fluorescence measurements of three plasma species with a tunable diode laser," Rev. Sci. Instrum. 75(10), 4091–4093 (2004).
- 45I. Romadanov and Y. Raitses, "A confocal laser-induced fluorescence diagnostic with an annular laser beam," Rev. Sci. Instrum. 94(7), 073002 (2023).
- 46I. Romadanov, A. Smolyakov, Y. Raitses, I. Kaganovich, T. Tian, and S. Ryzhkov, "Structure of nonlocal gradient-drift instabilities in Hall E × B discharges," Phys. Plasmas 23(12), 122111 (2016).
- 47]. Chen, A. T. Powis, I. D. Kaganovich, and Z. Wang, "Three-dimensional helical-rotating plasma structures in beam-generated partially magnetized E×B plasmas," arXiv:2501.01161 (2025).